



# A lead-free inorganic Cs<sub>2</sub>TiX<sub>6</sub>-based heterostructure perovskite solar cell design and performance evaluation

Md. Ashraful Islam<sup>1</sup> · Robi Paul<sup>2</sup>

Received: 28 April 2023 / Accepted: 27 July 2023 / Published online: 2 September 2023  
© The Author(s), under exclusive licence to Springer Science+Business Media, LLC, part of Springer Nature 2023

## Abstract

Perovskite materials are already showing their promising potential in solar cell development through their performance. To improve the performance to a greater extent, researchers have always explored different organic and inorganic materials compositions, among which CH<sub>3</sub>NH<sub>3</sub>PbI<sub>3</sub> is one of the most studied and analyzed. However, the popularity of lead (Pb) based perovskite materials has been held back in large-scale applications and the manufacturing industry due to its higher toxicity levels. Researchers turned to alternative lead-free inorganic perovskite materials for their comparative stability and non-toxic behaviors. This manuscript explores the performance of a lead-free Cs<sub>2</sub>TiX<sub>6</sub>-based n–i–p type heterostructure perovskite solar cell design performed using a one-dimensional device simulator, also known as the SCAPS-1D. Here, the design holds Cs<sub>2</sub>TiCl<sub>6</sub> as an n-type front absorber, Cs<sub>2</sub>TiI<sub>6</sub> as an I (intrinsic)-layer absorber and Cs<sub>2</sub>TiBr<sub>6</sub> as a p-type absorber. Again, NiO (p) and ZnO (n) are utilized as the hole transport material and electron transport material, respectively. The fluorine-doped tin oxide (FTO) acts as a front contact, conductive oxide, while Pt (platinum) is used as the back contact. Then the results of the proposed cell architecture were evaluated by varying parameters such as absorber thickness, doping concentration, work function for the back contact, various resistance types, operating temperature, and defect densities. After optimization, the fill factor (FF), device efficiency, open circuit voltage (V<sub>oc</sub>), and short circuit current density (J<sub>sc</sub>) for our device stands at 80%, 27.36%, 1.3505 V, and 24.707735 mA/cm<sup>2</sup>, respectively. Gaining a higher efficiency value of our solar cell while being lead-free inorganic material-based will surely give researchers a roadmap of future research directions.

**Keywords** Photovoltaics · Lead-free perovskite · Electron transport materials · Cs<sub>2</sub>TiX<sub>6</sub> · Cs<sub>2</sub>TiI<sub>6</sub> · Cs<sub>2</sub>TiCl<sub>6</sub> · Cs<sub>2</sub>TiBr<sub>6</sub> · Hole transport material · Absorber thickness · Doping concentration · Defect density · Device conversion efficiency (PCE)

---

✉ Robi Paul  
robipaul01733@gmail.com

<sup>1</sup> Department of Electrical and Electronics Engineering, Southeast University, Block B, House 64 Rd No 18, Dhaka 1213, Bangladesh

<sup>2</sup> Department of Electrical and Computer Engineering, Rochester Institute of Technology, One Lomb Memorial Dr., Rochester, NY 14623, USA

## 1 Introduction

Due to an overwhelming reliance on fossil fuels, the world has already begun to experience an energy crisis, placing the future in grave peril. As a solution to this imminent problem, scientists are now investigating alternative energy sources that are sustainable, limitless, and ecologically neutral. Solar electricity is one of the most plentiful energy sources presently accessible. Solar cells capture this energy and are considered sustainable and clean sources (Bhattacharya and John 2019; Grätzel 2014). Researchers are already exploring various material compositions to develop cost-effective and reasonably efficient devices for this purpose. Conventional silicon-based (C–Si) solar devices currently account for greater than 91% of the photovoltaic industry (Kour et al. 2019). This is because silicon is stable and good at turning light into electricity (PCE). Theoretically, in optimum room temperature situations, C–Si-based solar cell shows a conversion efficiency of 26.7% (Shockley and Queisser 1961). However, there are several problems as the fabrication process becomes expensive compared to real-life performance gain because of the indirect band gap, making it a weaker option for the longer wavelength of sunlight (Parida et al. 2011; Saive 2021).

The course of evolutions for the modern Solar cell designs like perovskite solar cells, also known as the PSCs, currently stands in the third generation of thin film photovoltaic (PV) technology (Chakraborty et al. 2019). Better physical, mechanical, and optoelectronic characteristics make perovskites a prime candidate for photovoltaic (PV) technology. Researchers have investigated both routes of single-layer and multi-layer absorber scenarios to maximize the overall performance. In the initial days of research, the cell architectures were a combination of organic–inorganic halide-based layers used as the absorber or the active layers (Ke and Kanatzidis 2019). Although those materials have conversion efficiencies above 20%, two significant issues still exist. The organic-based solar cells often have unstable organic cations, drastically shortening the device's self-life and performance. This makes the utilization of these categories of solar cells uneconomical. Additionally, lead (Pb), a hazardous substance, raises environmental issues due to its toxicity (Giustino and Snaith 2016). Again, some popular inorganic halide materials like Sn, Ag, Sb, Bi, and Cu contain a higher band gap of over 2 eV, making them less suited for photovoltaic devices (Snaith et al. 2014; Song et al. 2017). However, using inorganic materials as the cell's active materials also has drawbacks. For example,  $\text{Sn}^{2+}$  (Tin) cation contains a lower open-circuit voltage, the  $\text{Ge}^{2+}$  (Germanium) cation becomes unstable when it is oxidized, Bi (Bismuth) isn't good at moving charges, Sb (Antimony) has a low open-circuit voltage, Cu (Copper) doesn't work well as a photovoltaic, etc. To get around these problems, Chen and his team took a path towards Cesium Titanium (IV) Bromide based solar cell structure, which had a PCE of 3.28% (Chen et al. 2018). There they observed the band gap for the Cesium Titanium (IV) Halide materials could be altered between 1.4 and 1.8 eV, making them a good candidate for the Photovoltaic application. Again, it is previously noted that the diffusion length for both electron and hole carriers are equal for these compounds.

This study aimed to determine an optimal device setting for creating a hetero-junction solar cell using three perovskite active materials:  $\text{Cs}_2\text{TiBr}_6$ ,  $\text{Cs}_2\text{TiI}_6$ , and  $\text{Cs}_2\text{TiCl}_6$ . The materials were arranged in a specific order based on their bandgap, with  $\text{Cs}_2\text{TiCl}_6$  having the highest bandgap (2.23 eV) and serving as the upper layer.  $\text{Cs}_2\text{TiI}_6$  (1.8 eV) and  $\text{Cs}_2\text{TiBr}_6$  (1.6 eV) were placed sequentially, taking advantage of their progressively lower bandgaps. This arrangement allows for the efficient absorption of light across a wide range of wavelengths, maximizing the utilization of sunlight in a single junction solar cell.

## 2 Methodology

### 2.1 Research methodology

The simulation for this work was done through the SCAPS-1D, platform for solar cell design (Burgelman et al. 2000; Moustafa and Alzoubi 2018). It is a fairly generic software supporting modelling, numerical analysis, and monitoring of the photovoltaic structure's performance. The software allows adding up to seven distinct materials for building device structures. The simulator contains both single computation and batch computation functionality for the ease of its user. It is largely reliant on three fundamental equations: first, the Poisson's equation, following the 1-D continuity equations for electrons holes (Basak and Singh 2021; Burgelman et al. 2013),

$$\frac{d}{dx} \left( -\epsilon \frac{d\varphi}{dx} \right) = [p(x) - n(x) + N_D - N_A + \rho_p - \rho_n] \quad (1)$$

$$\frac{\partial p(x, t)}{\partial t} = -\frac{1}{q} \frac{\partial J_p}{\partial x} + G_p(x, t) - R_p(x, t) \quad (2)$$

$$\frac{\partial n(x, t)}{\partial t} = \frac{1}{q} \frac{\partial J_n}{\partial x} + G_n(x, t) - R_n(x, t) \quad (3)$$

Here  $n$  and  $p$  represent the concentrations for electron and hole for the materials. Again,  $N_A$  and  $N_D$  are the acceptors and donor doping density given at the doping stage, while  $n(x)$  and  $p(x)$  show the trapped electron density. The  $q$  and the  $\epsilon$  depict the material's charge and dielectric value of the medium.

Then if we cont, Carrier density for holes,

$$J_p = q \left[ p \mu_p E + D_p \frac{dp}{dx} \right] \quad (4)$$

and Carrier density for electrons,

$$J_n = q \left[ n \mu_n E + D_n \frac{dn}{dx} \right] \quad (5)$$

In steady-state requirements:  $\frac{\partial n}{\partial t} = 0$ . Hence from Eq. 3,

$$\frac{1}{q} \frac{\partial J_n}{\partial x} = -G_n(x, t) + R_n(x, t) \quad (6)$$

Then replacing  $J_n$  from Eq. 5. we have,

$$n \mu_n \frac{dE}{dx} + \mu_n E \frac{dn}{dx} + D_n \frac{d^2 n}{dx^2} = -G_n(x) + R_n(x) \quad (7)$$

Similarly, For Holes:

$$-p \mu_p \frac{dE}{dx} - \mu_p E \frac{dp}{dx} + D_p \frac{d^2 p}{dx^2} = -G_p(x) - R_p(x) \quad (8)$$

SCAPS can easily adapt many physical parameters as input, which can be further used in complex calculations to determine the performance aspect of the considered service against various parameters (Bal et al. 2022; Raj et al. 2020; Widiyanto et al. 2021).

### 2.2 Cell architecture and simulation parameters

The direction of our proposed Planer Heterostructure solar cell structure and the bandgaps for different materials utilized for this work is shown in Fig. 1. A basic description of the overall design can be represented as TCO/ETL/Absorber Layer/HTL. Here the TCO or Transparent Conducting Oxide layer represents a glass substrate or a window layer for the photons to pass through. We have used Fluorine doped Tin Oxide ( $\text{Sn}_2\text{O:F}$ ) (FTO) for this layer. The Electron Transport Layer (ETL) is a conductive layer where ZnO is chosen as an Electron transport Material (ETM) to extract electrons from the absorber before the recombination process is initiated. The absorber portion of the device is the accumulation of an n-i-p structure representing a tandem cell structure. Starting from the direction of the sunlight or the window layer, the first is the  $\text{Cs}_2\text{TiCl}_6$  which is an n-type absorber layer. The subsequent is a  $\text{Cs}_2\text{TiI}_6$  layer kept as intrinsic, and the last is  $\text{Cs}_2\text{TiBr}_6$ , which is a p-type layer used before the HTL. Finally, the HTL layer separates holes from the absorber layer, preventing absorption and increasing the device's overall efficiency. We choose NiO as our Hole transport Material (HTM) due to its greater hole conductivity and reasonable valance band and conduction band position having a better overall bandgap. The parameters list for all concerning layers utilized in the model are categorized in Tables 1, 2, 3, and Fig. 2 demonstrates the J-V characteristics curve for both Dark and Illumination cases obtained from the simulation process using the parameters. The designated values for these parameters are extracted from previously conducted experiments and theoretical works (Kumari et al. 2022; Moiz et al. 2022; Sabbah 2022) Other parameters like temperature, air mass, and light power were kept at 300 K, 1.5 ATM global, and  $1000 \text{ W/m}^2$ , respectively. Again, the absorption coefficient was taken using the equation below (Rai et al. 2020),

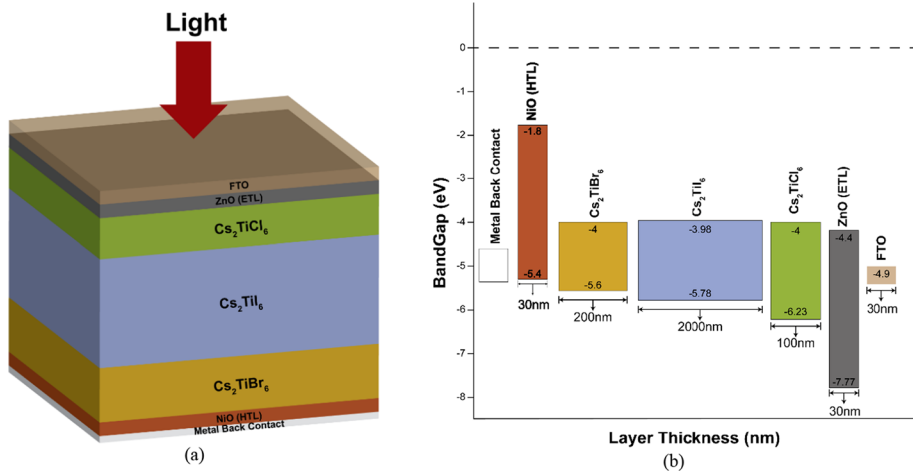


**Fig. 1** a 3-D schematic view of proposed solar cell structure, and b energy band diagram for the material sets

**Table 1** Parameters for different material layers used in the simulation process

Parameters	FTO	ZnO	Cs <sub>2</sub> TiCl <sub>6</sub>	Cs <sub>2</sub> TiI <sub>6</sub>	Cs <sub>2</sub> TiBr <sub>6</sub>	NiO
Thickness (μm)	0.03	0.03	0.1 (varied)	2 (varied)	0.2 (varied)	0.03
Bandgap, E <sub>g</sub> (eV)	3.50	3.37	2.23	1.80	1.60	3.60
Dielectric permittivity	9.00	10.00	11.90	18.00	10.00	11.70
Electron affinity, χ (eV)	4.00	4.35	4.02	4.20	4.47	1.80
Density of states-CB (cm <sup>-3</sup> )	2.20 × 10 <sup>18</sup>	2.20 × 10 <sup>18</sup>	1.00 × 10 <sup>18</sup>	1.00 × 10 <sup>18</sup>	2.20 × 10 <sup>18</sup>	2.50 × 10 <sup>20</sup>
Density of states-VB (cm <sup>-3</sup> )	1.80 × 10 <sup>18</sup>	1.78 × 10 <sup>19</sup>	1.00 × 10 <sup>19</sup>	1.00 × 10 <sup>19</sup>	1.60 × 10 <sup>19</sup>	2.50 × 10 <sup>20</sup>
Electron mobility, μ <sub>n</sub> (cm <sup>2</sup> /V s)	20	100	4.4	4.4	2.5	2.8
Hole mobility, μ <sub>p</sub> (cm <sup>2</sup> /V s)	10	50	2.5	2.5	2.5	2.8
Donor concentration, N <sub>D</sub> (cm <sup>-3</sup> )	1.00 × 10 <sup>20</sup>	1.00 × 10 <sup>20</sup>	1.00 × 10 <sup>16</sup> (varied)	0	0	0
Acceptor concentration, N <sub>A</sub> (cm <sup>-3</sup> )	0	0	0	0	1.00 × 10 <sup>20</sup> (varied)	1.00 × 10 <sup>20</sup>

References Chakraborty et al. (2019), Chen et al. (2018), Paul et al. (2018), Ju et al. (2018), and Chaudhary et al. (2015)

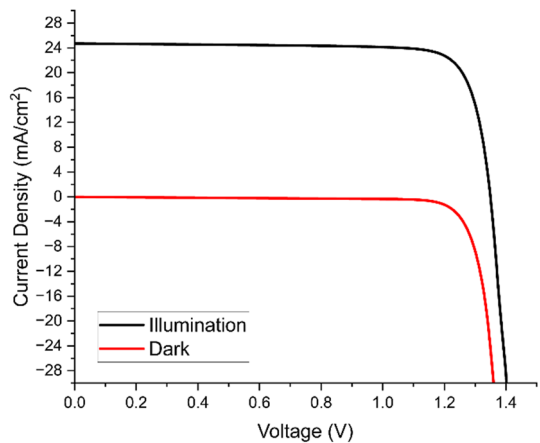
**Table 2** Parameters for different HTM materials for the HTL layer

Parameters	SrCu <sub>2</sub> O <sub>2</sub>	CuSbS <sub>2</sub>	Cu <sub>2</sub> O	Nio
Thickness (μm)	0.03	0.03	0.03	0.03
E <sub>g</sub> (eV)	3.3	1.58	2.17	3.6
Permittivity	9.7	14.6	7.5	11.7
χ (eV)	2.2	4.2	3.2	1.8
N <sub>c</sub> (cm <sup>-3</sup> )	2.20 × 10 <sup>18</sup>	2.00 × 10 <sup>18</sup>	2.00 × 10 <sup>18</sup>	2.50 × 10 <sup>18</sup>
N <sub>v</sub> (cm <sup>-3</sup> )	1.80 × 10 <sup>18</sup>	1.00 × 10 <sup>19</sup>	1.80 × 10 <sup>19</sup>	2.50 × 10 <sup>20</sup>
N <sub>D</sub> (cm <sup>-3</sup> )	0	0	0	0
N <sub>A</sub> (cm <sup>-3</sup> )	1.00 × 10 <sup>20</sup>	1.00 × 10 <sup>20</sup>	1.00 × 10 <sup>20</sup>	1.00 × 10 <sup>20</sup>
μ <sub>n</sub> (cm <sup>2</sup> /V s)	0.1	49	20	2.8
μ <sub>p</sub> (cm <sup>2</sup> /V s)	0.46	49	80	2.8

**Table 3** Parameters for different ETM materials for the ETL layer

Parameters	PCBM	CdS	ZnSe	ZnO
Thickness (μm)	0.03	0.03	0.03	0.03
E <sub>g</sub> (eV)	2.0	2.4	2.81	3.37
Permittivity	3.9	10	8.6	10.00
χ (eV)	4.0	4.18	4.09	4.35
N <sub>c</sub> (cm <sup>-3</sup> )	2.50 × 10 <sup>21</sup>	2.20 × 10 <sup>18</sup>	2.20 × 10 <sup>18</sup>	2.20 × 10 <sup>18</sup>
N <sub>v</sub> (cm <sup>-3</sup> )	2.50 × 10 <sup>21</sup>	1.78 × 10 <sup>19</sup>	1.78 × 10 <sup>19</sup>	1.78 × 10 <sup>19</sup>
N <sub>D</sub> (cm <sup>-3</sup> )	1.0 × 10 <sup>20</sup>	1.0 × 10 <sup>20</sup>	1.0 × 10 <sup>20</sup>	1.0 × 10 <sup>20</sup>
N <sub>A</sub> (cm <sup>-3</sup> )	0	0	0	0
μ <sub>n</sub> (cm <sup>2</sup> /V s)	0.2	100	400	100
μ <sub>p</sub> (cm <sup>2</sup> /V s)	0.2	25	110	50

**Fig. 2** J–V characteristic curve with and without illumination for proposed cell



$$\alpha(E) = \left( \alpha_0 + \beta_0 \frac{E_g}{hv} \right) \sqrt{\frac{hv}{E_g} - 1} \quad (9)$$

Here  $\alpha(h\nu)=0$  for  $h\nu < E_g$ ,  $\alpha_0=10^5$  and  $\beta_0=10^{12}$  was kept during the simulation process. However, despite all the parameters mentioned above, for all defects, Gaussian defect distribution is considered while the type is considered as natural with the characteristics value of 0.1 eV.

The study contains a comprehensive investigation of the perovskite cell's performance by changing the materials for different layers, altering the thickness of the layers, the impacts of doping concentration, the density of defects present in the absorption layer, and the effects of operating temperature. Here the graphs containing current density vs voltage characteristics with the addition of short-circuit current density ( $J_{sc}$ ), open circuit voltage ( $V_{oc}$ ), Fill Factor (FF), and Power Conversion Efficiency (PCE) are also represented. At the end of the optimization process with the desired material sets and parameters, we were able to achieve  $J_{sc}$ , ( $V_{oc}$ ), FF and an overall Device Efficiency value of 24.707735 mA/cm<sup>2</sup>, 1.3505 V, 80%, and 27.36% respectively.

The results are close to one of the most recent experimental results on Cesium-Based Lead-Free inorganic perovskite solar cell (Raj et al. 2022). The observation, therefore, verifies the legitimacy of proposed simulated device's output and the compatibility of the parameters assigned for the optimization process.

### 3 Performance investigation and discussion

#### 3.1 Variation of work function for the back contact of the proposed device structure

This part investigates the impact of work function modification for the back contact over the performance characteristics of proposed simulated device model. Theoretically, a higher work function will reduce the height of the barrier of the majority carrier, turning the contact into ohmic. Thus, increasing metal work function can improve the overall efficiency, Fill factor, and short circuit current while bringing down the open circuit voltage. Over the years, a lot of investigation has been done containing different material sets and observing the cell design's performance. Here Table 4 represents a set of materials with their respective work functions that are considered for this study. All these parameters are

**Table 4** Work functions of different metals used as back contact in proposed PSCs

Metal	Work function (eV)	PCE (%)
Au	4.6	7.385
Ag	4.7	9.215
Fe	4.8	11.079
Nb	4.9	12.97
Cu-graphite alloy	5	14.88
Au	5.1	16.806
Ni	5.5	21.925
Pt	5.7	21.937

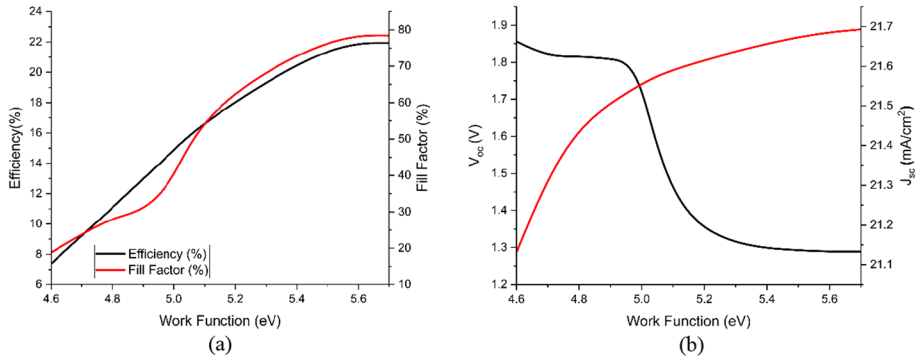


**Fig. 3** Impacts of work function variation on the proposed cell

collected from previously conducted theoretical and experimental studies (Sawicka-Chudy et al. 2019). Again, Fig. 3 depicts the performance aspects of the simulated device model over the change of work functions. The graph shows that increasing the work function is improving the overall efficiency value, Fill factor, and short circuit density value of the device up to the use of the Platinum (Pt). The open circuit voltage is also seen to improve throughout changes. Given these findings, we selected Pt as a back contact material. Thus, the findings offer experimentalists quantitative certainty in choosing the appropriate back-contact material.

### 3.2 Variation of the absorber layers on the proposed device structure

The absorber layer is a semiconducting substance often regarded as the heart and soul of all solar cell design variations. The name is well justified as the layer is responsible for absorbing the maximum amount of photons and generating electron–hole pairs that are later responsible for the current flow. When a photon with an energy level equal to or higher than the material’s bandgap is indented, the electron will gain energy to reposition itself in the conduction band. So, choosing the semiconducting materials with bandgaps that match the photon-dense area of the sunlight is a mandatory point to ensure the better performance of any cell structure. However, the performance of any device also depends on the overall material properties. This study proposes an n–i–p structure in the absorber layer containing materials of n- $\text{Cs}_2\text{TiCl}_6$ , i- $\text{Cs}_2\text{TiI}_6$  and p- $\text{Cs}_2\text{TiBr}_6$ . The multilayer solar cells normally have more flexibility towards absorbing wavelengths of different ranges giving an edge over the single-layer variants. The added amount of photo-generated electron increases the fill factor, and short circuit currents ultimately uplift the device’s overall efficiency. Here, Table 1 contains all the necessary parameters for proposed solar cell structure simulation. Subsequently, we have analyzed each layer individually against proposed structure. Figure 4 depicts the effects of using the proposed materials as a single layer against proposed structure, and Table 5 shows the PV parameters of the devices. Here we can see that although our proposed structure of FTO(TCO)/ZnO (ETL)/n- $\text{Cs}_2\text{TiCl}_6$ /i- $\text{Cs}_2\text{TiI}_6$ /p- $\text{Cs}_2\text{TiBr}_6$ /NiO (HTL)/Pt (Back contact) shows a better performance in every case. But in the case  $\text{Cs}_2\text{TiCl}_6$ , we have observed the lowest values in all PV parameters except the  $V_{oc}$  having the highest value of 2.10 V. It is because of the high bandgap of the  $\text{Cs}_2\text{TiCl}_6$  being 2.23 eV. Moreover, the proposed



**Fig. 4** J–V characteristic curve for different absorber layer scenarios for proposed solar cell

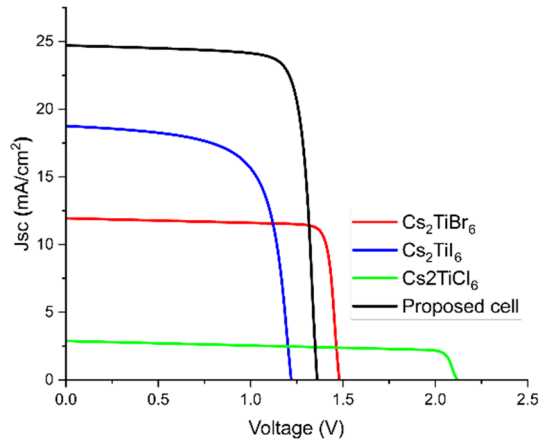


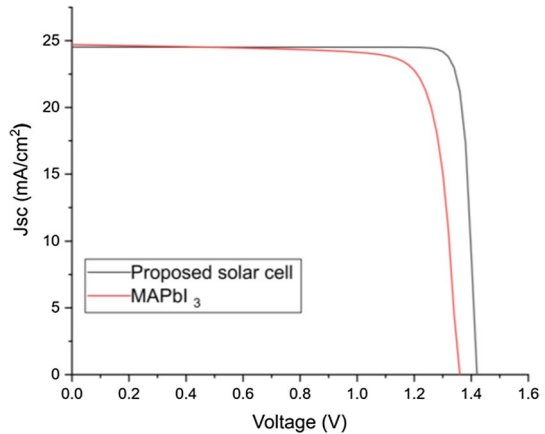
**Table 5** PV parameters for using different absorber layers

Solar cell	Efficiency (%)	FF (%)	V <sub>oc</sub> (V)	J <sub>sc</sub> (mA/cm <sup>2</sup> )
FTO/ZnO(n)/Cs <sub>2</sub> TiCl <sub>6</sub> /NiO(p)/Pt	4.35	71.89	2.10	2.87
FTO/ZnO(n)/Cs <sub>2</sub> TiI <sub>6</sub> /NiO(p)/Pt	15.65	68.759	1.21	18.75
FTO/ZnO(n)/Cs <sub>2</sub> TiBr <sub>6</sub> /NiO(p)/Pt	15.24	86.98	1.47	11.94
FTO/ZnO(n)/n-Cs <sub>2</sub> TiCl <sub>6</sub> /i-Cs <sub>2</sub> TiI <sub>6</sub> /p-Cs <sub>2</sub> TiBr <sub>6</sub> /NiO(p)/Pt (proposed)	27.36	82.00	1.35	24.70

solar cells' overall performance is considerably higher than those using the materials individually. As such, we have continued the further study using the proposed structure as our intended device.

Although this manuscript covers the lead-free implementation, in the initial days of the high-efficiency device designs, the lead-based materials were widely utilized due to their inexpensive cost. However, the use of lead in solar cells has prompted concerns regarding the environmental impact of these devices, as lead is a hazardous material that, if improperly handled, can pose threats to human health and the environment. This imposes the lead-free alternatives to be a considerable container considering the environmental uses. Then again, the lead tends to react with other materials within the cell, which can lead to corrosion and deterioration over time. This causes a decline in the cell's efficiency and may finally lead to the cell's demise. The lead-based designs are often subjective to vulnerable environmental conditions such as temperature, humidity, and light exposure, which may accelerate the degradation of cell components. In contrast, the Lead-free perovskite cell designs are typically more stable and have a longer lifespan. They are also less susceptible to deterioration and better able to handle environmental conditions. Lead-free perovskite solar cells can also be manufactured on a larger scale than lead-healed perovskite solar cells, as the toxicity of lead poses threats to human health and the environment if not handled appropriately. Often, countries impose rules and norms to guarantee the safe handling and disposal of lead-containing components, which makes scaling up the manufacture of lead-based solar cells more difficult. Using a J–V curve, Fig. 5 depicts a comparison between a

**Fig. 5** J–V characteristic curve for lead-based absorber layer scenarios with proposed solar cell

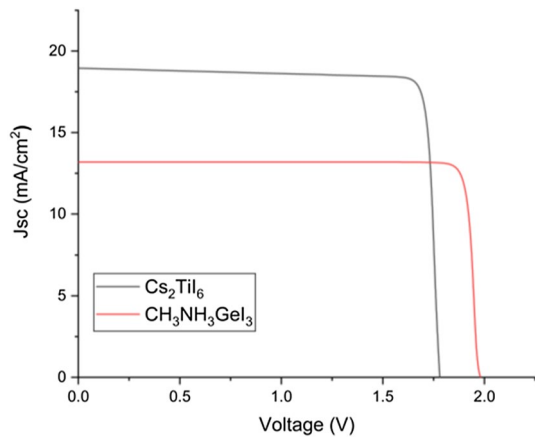


lead-based solar cell design using  $\text{MAPbI}_3$  as the absorber layer and our suggested design. Here, we can see that the suggested design yields superior performance outcomes while also providing the previously outlined advantages.

Furthermore, incorporating numerous variations of the perovskite crystal structure may affect the device's performance characteristics. Single and double perovskite materials are one of the recent choices for high-efficiency solar cell research.  $\text{ABX}_3$  can be regarded as the general formula for the single perovskite materials, where A is a cation (Ion with a positive charge), B represents a distinct cation, where X stands for an anion (negatively charged ion). The cation B is usually positioned in the cube's center, while the A cation and X anion are at the cube's corners. Due to their more straightforward crystal structure, single perovskite-based solar cells are more suited for scaling due to their easier manufacture. However, the materials are often degraded within a shorter period, reducing their usability. In these situations, the double perovskite can be a suitable alternative. The typical formula for double perovskites is  $\text{A}_2\text{BB}'\text{O}_6$ , where the notation A is a cation, B and B' are distinct cations, where O stands for an anion. In this sequence, the two B cations occupy the cube's center, while the A cation and the O anion occupy the cube's corners. Despite the complicated structure, the implementation of the double perovskite has some advantages over the single one. Firstly, the double perovskite cell designs are more immune to environmental effects such as heat and moisture. These devices also contain high open circuit voltage and a broad spectrum for the absorption process. Figure 5 compares the single and double perovskite used as the absorption layer. Due to its broad-spectrum coverage, the three-layer absorption part of the proposed device is expected to improve performance. As a result, we have exclusively selected  $\text{Cs}_2\text{TiI}_6$  as the double perovskite material to demonstrate the performance advantages of using double perovskite. In terms of Efficiency, Fill Factor, Open Circuit Voltage, and Short Circuit Current, Table 6 then compares the performance of the two absorber layers. To provide an exact comparison, despite the absorber layers, all other layers are maintained in the same configuration. In accordance with Fig. 6, the table also depicts the performance enhancements of the double perovskite material over the single variant in each instance.

**Table 6** PV parameters for using different absorber layers

Solar cell	Efficiency (%)	FF (%)	V <sub>oc</sub> (V)	J <sub>sc</sub> (mA/cm <sup>2</sup> )
FTO/ZnO(n)/ Cs <sub>2</sub> TiI <sub>6</sub> / NiO(p)/Pt	15.65	68.759	1.21	18.75
FTO/ZnO(n)/ CH <sub>3</sub> N- H <sub>3</sub> GeI <sub>3</sub> / NiO(p)/Pt	23.96	92.62	1.96	13.18

**Fig. 6** J–V characteristic curve for single (CH<sub>3</sub>NH<sub>3</sub>GeI<sub>3</sub>) and double (Cs<sub>2</sub>TiI<sub>6</sub>) perovskite materials as the absorber layer

### 3.3 Variation of the absorber thickness for the proposed device

The subsection analyses the proposed solar cell's performance by altering the layer thickness of the three intended absorbing layers and finding stability according to the output results. The thickness of the absorbing layer has to be considered a significant point in the performance optimization process, as it can directly affect the diffusion length of the charged carriers. As per previous observation, we can determine that the absorption rate of the absorbing layer is poor at lower thickness due to lower photocurrent, which can badly affect the PCE of the device (Correa-Baena et al. 2016; Lin et al. 2017). In contrast, higher thickness exceeding a point is also a drawback for any cell, which can result in an unwanted higher series resistance value within the cell and bring down the efficiency of the device. The effect can be observed through the graph of V<sub>oc</sub> and FF, where it decreases after a certain point because of increasing recombination and series resistance in the perovskite absorber layer. Consequently, at the end of the section, an optimal thickness of the individual absorbing layer is considered according to the output parameters received from the simulation process (Lin et al. 2017; Huang et al. 2017).

Figure 7 illustrates the effects of absorber layer thickness variation using the Batch-Calculation and Recorder function of SCAPS-1D. The performance and the optimization process for the depth of each absorber layer were carried out keeping the doping concentration at  $1 \times 10^{22} \text{ cm}^{-3}$  for p and n-type doping layers and  $1 \times 10^{16} \text{ cm}^{-3}$  for the intrinsic layer throughout. During the simulation, the n-type Cs<sub>2</sub>TiCl<sub>6</sub> layer was varied 0.02–3  $\mu\text{m}$

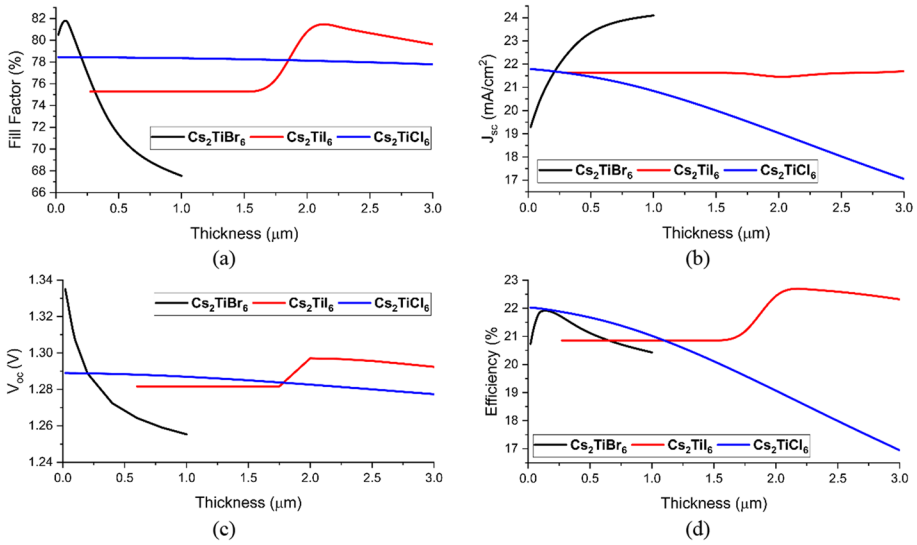


**Fig. 7** Impact of thickness variation of the absorber layer for the proposed cell

which left an effect seen through the figure. A linear decrease rate is seen in the case of the device’s overall efficiency from 22 to 16%. The Short Circuit Current Density ( $J_{sc}$ ) has also been decreasing from 21 to 17 mA/cm<sup>2</sup>. Next for intrinsic i-Cs<sub>2</sub>TiI<sub>6</sub> absorber, we have varied thickness form 0.2–3 μm. Here we observed a rapid increment in efficiency and FF after thickness 1.7 μm and reached a peak value of 22.8% and 82%, respectively. The Open circuit Voltage ( $V_{oc}$ ) also experiences a sudden change during this time. However, after 2 μm thickness, the  $V_{oc}$  declines, which results in a fall down of efficiency and FF reaching 20% and 80%, respectively, as recombination current and series resistance starts to increase into the bulk region of the absorber. Finally, the p-Cs<sub>2</sub>TiBr<sub>6</sub> layers thickness was varied from 0.02 to 1 μm. Due to the increase in thickness, we can see an increment in efficiency and FF till 0.1 μm reached 22% and almost 82%, respectively. There is also a significant rise in  $J_{sc}$  due to the absorption of a higher amount of photons, ultimately increasing the carrier generation. However, with further increasing depth of this layer, the efficiency and FF start to decrease at 20.45% and 67.5%, respectively. The  $V_{oc}$  also decreases from a peak value of 1.35–1.25 V. The explanation can be understood by the reasoning of charge carriers to be recombined within the absorber before they reach the metal contact. The effects also cause an increase in the value of series resistance. Here the correlation between the ( $J_{sc}$ ) and ( $V_{oc}$ ) can be expressed through the Eq. 10 (Mandapau et al. 2017), as follows:

$$V_{oc} = \frac{k_B T}{q} \ln \left( \frac{J_{sc}}{J_0} + 1 \right) \tag{10}$$

Here ( $J_{sc}$ ) represents the Short Circuit Current Density, and ( $J_0$ ) shows the value of the Reverse Saturation Current. The  $q$  is the electronic charge, and  $T$  is the device’s operating temperature. Again,  $k_B$  shows the Boltzmann constant. In this situation, the thickness value of the highest efficiency and other values are considered for this device’s optimized version and carried up to future investigations. The following Table 7 shows the optimum thickness and the values of the considered parameters for the performance investigation.

**Table 7** Impacts of different absorbing layer's optimum thickness on corresponding parameters

Layers	Optimum thickness ( $\mu\text{m}$ )	Efficiency (%)	FF (%)	$V_{oc}$ (V)	$J_{sc}$ ( $\text{mA}/\text{cm}^2$ )
n-Cs <sub>2</sub> TiCl <sub>6</sub>	0.1	22	78.44	1.29	21.75
i-Cs <sub>2</sub> TiI <sub>6</sub>	2	22.8	82.05	1.3	21.4
p-Cs <sub>2</sub> TiBr <sub>6</sub>	0.2	21.9	78.43	1.29	21.69

### 3.4 Variation of various ETM and HTM layers

This subsection demonstrates the observation of the different outcomes gained through the simulation process by altering different ETM and HTM materials on proposed cell structure and determining a possible option according to their performance. In a perovskite solar cell, an active absorber layer is often placed between an Electron Transport Material (ETM) and a Hole Transport Material (HTM). The goal is to separate the electron and hole generated by an incident photon with sufficient energy before the recombination process occurs. So, the ETM and the HTM materials are to be chosen such that the ETM has a higher work function than the HTM, creating an internal electric field in the active region directing from ETL to the HTL. The built-in electric field then separates the generated electron and hole and moves them toward the ETL and HTL layers to be collected. Again, the carrier mobility for both material sets also has an essential effect in determining the overall performance of the cell structure. For having an equal visualization of performance aspects, the thickness, donor, and acceptor doping concentrations are kept the same for all materials.

Initially, the HTL material is taken to be investigated where we have candidates like NiO, SrCu<sub>2</sub>O<sub>2</sub>, CuSbS<sub>2</sub> and Cu<sub>2</sub>O where the thickness of each layer is taken as 0.03  $\mu\text{m}$ . This makes the structure for proposed device as FTO(TCO)/ZnO(ETL)/n-Cs<sub>2</sub>TiCl<sub>6</sub>/i-Cs<sub>2</sub>TiI<sub>6</sub>/p-Cs<sub>2</sub>TiBr<sub>6</sub>/(HTM Materials)/Pt(Back contact). The properties of these considered values are listed in Table 2, where the values are collected from previously demonstrated experimental and theoretical manuscripts (Sawicka-Chudy et al. 2018; Singh et al. 2021).

**Fig. 8** J–V characteristic curve for different HTL layers

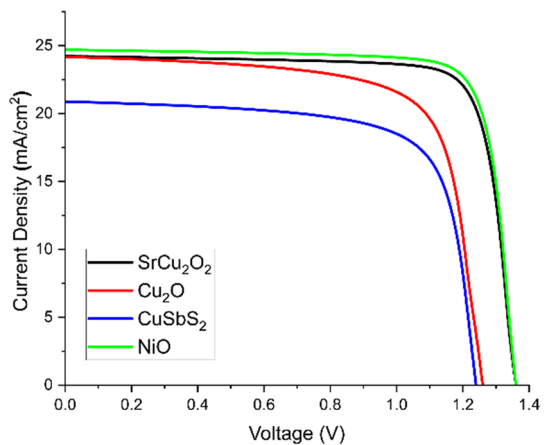


**Table 8** Impacts of various HTM on the PV parameters

ETL/HTL	Efficiency (%)	FF (%)	V <sub>oc</sub> (V)	J <sub>sc</sub> (mA/cm <sup>2</sup> )
ZnO/SrCu <sub>2</sub> O <sub>2</sub>	27.00	81.00	1.34	24.22
ZnO/Cu <sub>2</sub> O	21.94	73.03	1.24	24.18
ZnO/CuSbS <sub>2</sub>	18.72	72.66	1.23	20.88
ZnO/NiO	27.36	82.00	1.35	24.70

Figure 8 illustrates the J–V curve using different materials as the HTL layer, whereas Table 8 shows the PV parameters for those material sets. Here we can observe that the highest value of J<sub>sc</sub> and V<sub>oc</sub> is seen for the NiO standing at 24.7 mA/cm<sup>2</sup> and 1.35 V, respectively. The material also shows a better performance in terms of efficiency and FF, having a value of 27.36% and 82%. The reason behind such high ground against the other alternatives can be taken as the larger bandgap among the others.

As per the HTL layer, the ETL layers are also approached similarly. For this case, the simulation candidates are PCBM, CdS, ZnSe, and ZnO. Like the previous case, the thickness and doping concentrations are kept similar for equal comparison, the thickness for the simulation was kept at 0.03 μm, and the concentration was at 1 × 10<sup>20</sup>. The structure for this case stands as, FTO(TCO)/(ETM Materials)/n-Cs<sub>2</sub>TiCl<sub>6</sub>/i-Cs<sub>2</sub>TiI<sub>6</sub>/p-Cs<sub>2</sub>TiBr<sub>6</sub>/NiO(HTL)/Pt(Back contact). Table 3 shows all necessary parameters for the material sets collected from previously analyzed theoretical and experimental manuscripts. Again Fig. 9 and Table 9 illustrate the J–V curve for different ETL materials and PV parameters for those material sets. Here we can see that ZnO shows competitively better performance. The J<sub>sc</sub> and the V<sub>oc</sub> are seen to be 24.70 mA/cm<sup>2</sup>, and 1.35 V respectively whereas the FF and the efficiency for the ZnO are 82% and 27.36%. The reasoning for these performance

**Fig. 9** J–V characteristic curve for different ETL layers

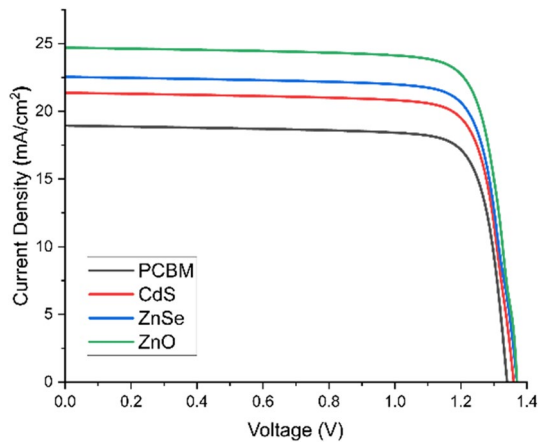


**Table 9** Impacts of various ETM on the PV parameters

ETL/HTL	Efficiency (%)	FF (%)	V <sub>oc</sub> (V)	J <sub>sc</sub> (mA/cm <sup>2</sup> )
PCBM/NiO	20.74	81.87	1.33	18.94
CdS/NiO	23.52	81.94	1.34	21.36
ZnSe/NiO	24.87	81.96	1.34	22.54
ZnO/NiO	27.36	82.00	1.35	24.70

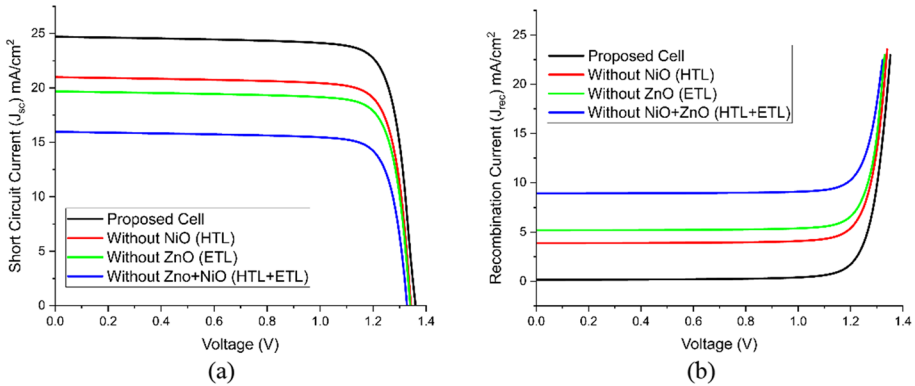


**Fig. 10** **a**  $J_{sc}$ - $V$  curve, **b**  $J_{rec}$ - $V$  curve for different scenarios of HTL and ETL layer presence

**Table 10** Impact of different scenarios of HTL and ETL layer effects on the PV parameters

Layers	$J_{sc}$ (mA/cm <sup>2</sup> )	Initial $J_{rec}$ (mA/cm <sup>2</sup> )	$V_{oc}$ (V)	FF (%)	Efficiency (%)
Without NiO (HTL)	20.99	3.88	1.34	81.70	23.02
Without ZnO (ETL)	19.68	5.18	1.34	81.89	21.58
Without NiO + ZnO (HTL + ETL)	15.90	9	1.32	81.43	17.27
Proposed cell	24.70	0.155	1.35	82.00	27.38

gaps is similar to the HTL layer’s case because ZnO has a higher bandgap than others and also competitive carrier mobility. As per the results, we then chose ZnO as the ETM which gives the cell structure as, FTO(TCO)/ZnO(ETL)/n-Cs<sub>2</sub>TiCl<sub>6</sub>/i-Cs<sub>2</sub>TiI<sub>6</sub>/p-Cs<sub>2</sub>TiBr<sub>6</sub>/NiO(HTL)/Pt(Back contact).

Although the ETL and HTL layers are an essential part of determining the performance of a PSC acting as a separator of electrons and holes generated at the active layer, the impact of these layers’ existence and different permutation scenarios are also needed to be analyzed. The study reveals the importance of these layers and shows the effects on the performance due to the absence of any or both layers against the proposed model. Here, the short circuit recombination current ( $J_{rec}$ ) is called the initial recombination current at which voltage is 0 V and is the determiner of sell performance as it has an inverse relation with short circuit current ( $J_{sc}$ ).

The effects of HTL and ETL layers are demonstrated in Fig. 10 and Table 10. Here, Fig. 10a depicts the  $J_{sc}$ - $V$  curve for proposed solar cell structure in various HTL and ETL configurations, whereas Fig. 10b depicts the short circuit recombination current for the same. Table 10 represents the PV parameters of the simulated device with various HTL and ETL permutations. For the proposed solar cell structure, we were able to achieve nearly 24.70 mA/cm<sup>2</sup> of  $J_{sc}$ , 1.35 V of  $V_{oc}$ , 82% of FF, and PCE of 27.36% while having lowest 0.155 mA/cm<sup>2</sup> of  $J_{rec}$  (recombination current density). After removing the HTL(NiO) layer, all parameters take a hit, especially since the efficiency comes down to only 23.03%. The value of the ( $J_{sc}$ ) also comes down to 21 mA/cm<sup>2</sup> and the recombination current ( $J_{rec}$ ) rises

up to  $3.88 \text{ mA/cm}^2$ . The reasoning is the lack of proper hole separation due to the lack of the HTL layer. Again, when the ETL(ZnO) layer is stripped away from the cell, the PV parameters are dragged down even lower, showing values like PCE of 21.58%,  $J_{sc}$  value of  $19.68 \text{ mA/cm}^2$  and  $J_{rec}$  value of  $5.18 \text{ mA/cm}^2$ . In the case of the ETL removal in place of the HTL layer, the effects of electron carriers are more severe in the cell performance than the effects of hole carriers. Again, removing both HTL and ETL layers brings down the performance parameters even more. A decrease of PCE is around 10% compared to the proposed structure being only at 17.27%. The short circuit current density ( $J_{sc}$ ) also severely comes down to a value of  $15.96 \text{ mA/cm}^2$ , and the current recombination density peaked at the value of  $9 \text{ mA/cm}^2$ . Due to the absence of HTL and ETL layers, there is no separator of the hole and electron to pull out from the absorber layer following the electron–hole pair formation process. The situation then escalates into the majority of electrons recombining with holes within the cell, bringing down the overall performance.

### 3.5 Variation of doping concentration in the absorber layers

This subsection summarizes the performance parameter alteration that occurs due to the changes in doping densities in the absorbing layers. Doping is a crucial parameter that controls the performance spectrum of any solar cell design. Depending on the type, the material characteristics can positively and negatively impact the overall device (Schloemer et al. 2019). So, optimization of the doping concentration in the absorbing layers to achieve a higher level of efficiency is a crucial point. Studies have already shown that an unoptimized or unwanted amount of doping concentration can affect the overall carrier density and introduce uncertain defects, limiting the carriers' transportation. The effect then alters the stability of the device and brings down the overall power conversion efficiency (PCE). To have a clear view of the doping effects on the cell performance, we have varied the concentration from  $1 \times 10^{10}$  to  $1 \times 10^{22}$  to observe the effects of both high and lower doping

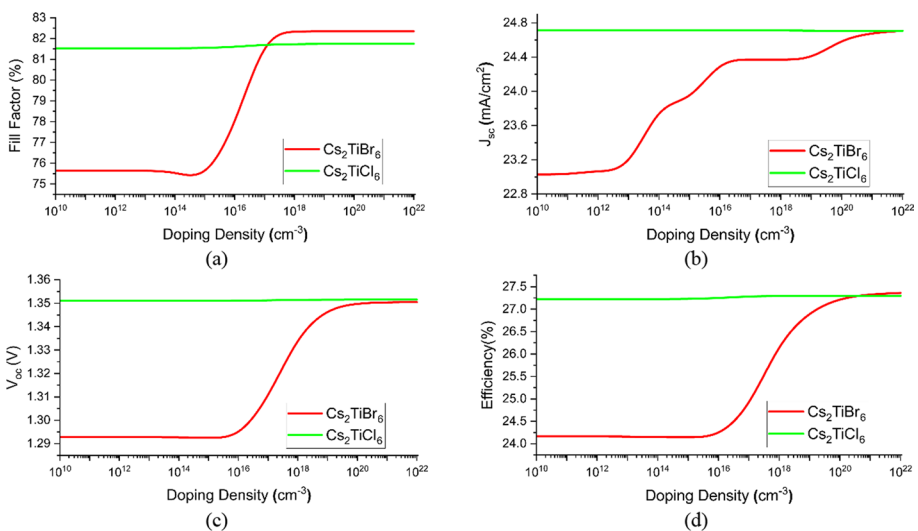


**Fig. 11** Impact of doping concentration variation of the proposed cell's absorber layer



densities. Again, in this study, the doping concentration is altered for both of the material sets naming the n-Cs<sub>2</sub>TiCl<sub>6</sub> and p-Cs<sub>2</sub>TiBr<sub>6</sub>. But as Cs<sub>2</sub>TiI<sub>6</sub> is kept as an intrinsic layer, it is not considered for this study. Here, Fig. 11 depicts the changes in performance metrics due to the alteration of the absorber layer's doping concentration. The simulations are conducted with each of the absorber layer thicknesses set to their ideal values, which indicates the swept of doping concentration will surely give a point of stability at the end of the process. Here the graph reveals that up to a doping concentration of  $1 \times 10^{16}$  the PV parameters for the p-Cs<sub>2</sub>TiBr<sub>6</sub> somewhat stay stable. But exceeding this point shows an exponential improvement in the results up to  $1 \times 10^{20}$ . However, although the results don't show an exponential increase from this point, there is a linear increase in performance with increasing doping concentration for Cs<sub>2</sub>TiBr<sub>6</sub>. In the end, at a doping concentration of  $1 \times 10^{20}$ , we can see that the short circuit current density is at 24.707 mA/cm<sup>2</sup> while the Fill Factor is at 82.347%. Again, the efficiency and the open circuit voltage ( $V_{oc}$ ) are 27.363% and 1.35 V, respectively. The doping concentration of the n-Cs<sub>2</sub>TiCl<sub>6</sub> has seen less of an effect due to the changes in the doping concentrations. The material has been seen to be almost linear with a slight improvement at the  $1 \times 10^{16}$  mark in all the parameters. As such a stable doping concentration of  $1 \times 10^{20}$  is considered for the p-Cs<sub>2</sub>TiBr<sub>6</sub> and a doping concentration of  $1 \times 10^{16}$  is taken for n-Cs<sub>2</sub>TiCl<sub>6</sub>.

### 3.6 Variation of defect densities at the absorber layers

In the architecture of a solar cell design, the absorber layer is considered an essential part of most photovoltaic operations, including electron-hole pair generation, recombination, and carrier transport, which initially occurred inside this layer. Numerous articles and research have demonstrated that the overall quality and molecular chemistry and the impact of the fabrication process of an absorber layer can significantly impact the device's performance by reducing the total lifespan and the diffusion length for carriers (Ball et al. 2013; Barbe et al. 2017; Kim et al. 2016). Subsequently, the defect density can have a critical role in controlling the performance parameters of a structure, so modifying the defect density to an optimum value is necessary for enhancing the device's overall performance. During the simulation stage, the defect densities in the absorber layer may often be omitted due to ease during the calculation process. However, defects can be introduced during fabrication, affecting performance parameters. So, a specific number of imperfections must be introduced to have near-realistic results. Here, Fig. 12 depicts the effects over the Fill Factor, efficiency, and other PV parameters by alternating defect density ranging from  $1 \times 10^{10}$  to  $1 \times 10^{22}$  cm<sup>-3</sup>.

Traditional cases, during the fabrication process, the material sets are bound to have defects normally in the  $10^{14}$ . So, although lower defect densities are bound to show better performance in every PV parameter to have a more realistic real-life output scenario, we have considered  $1 \times 10^{15}$  cm<sup>-3</sup> as optimum range for this simulation. So, when the defect densities are varied in one absorbing layer, in other layers, the densities are kept at a fixed position of  $1 \times 10^{15}$  cm<sup>-3</sup>. When we have varied the defect density of the p-Cs<sub>2</sub>TiBr<sub>6</sub> the highest level of performance with a PCE of 27.42% and a Fill Factor of 82.01% is seen for the defect density of  $1 \times 10^{10}$  cm<sup>-3</sup>. Despite the downward trends in the efficiency curve, the defects in the Cs<sub>2</sub>TiBr<sub>6</sub>, when increased are, showing very few changes and almost hold a constant value in all cases with minimal changes. So, a stable position of considerable defect density for the p-Cs<sub>2</sub>TiBr<sub>6</sub> is taken as  $1 \times 10^{15}$  cm<sup>-3</sup>. Likewise, the p-Cs<sub>2</sub>TiBr<sub>6</sub> material the n-Cs<sub>2</sub>TiCl<sub>6</sub> also shows minimal alteration with

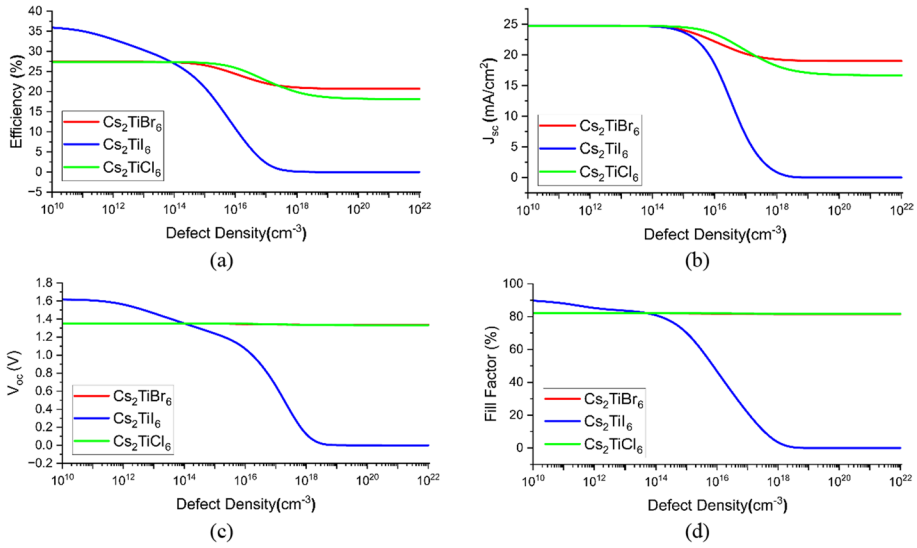


**Fig. 12** Effects of defect densities for various absorber layer of the proposed cell

the variation in defect density. So, the stable position for the n-Cs<sub>2</sub>TiCl<sub>6</sub> is also taken at the point of  $1 \times 10^{15} \text{ cm}^{-3}$ . Finally, in the case of the i-Cs<sub>2</sub>TiI<sub>6</sub>, the change in defect density is more severe. As usual, it shows the best results in lower defects densities of  $1 \times 10^{10} \text{ cm}^{-3}$  where the value of the PCE is 35.93%, and the Fill Factor standing in 89.74%. However, after the value of  $1 \times 10^{15} \text{ cm}^{-3}$ , an abrupt change in the performance aspects is seen as all parameters are seen to have an exponential fall with increasing defect densities eventually reaching a minimal point near the mark of  $1 \times 10^{18} \text{ cm}^{-3}$ . Due to the influence of defect densities present in the absorber layers of a cell design, the lifespan and the diffusion length of the carriers takes a great hit. Due to the poor quality of the fabrication process or due to the material’s molecular properties, when a significant amount of defect densities is introduced inside or between the layers, the majority of the generated carriers, due to the photogeneration process, recombine. This reduces the short circuit current density ( $J_{sc}$ ), ultimately downgrading the overall device performance. Shockley–Read–Hall, in his study of the recombination model, also known as the SRH model, has shown the effects that the defect density of an absorber layer has on the performance parameters of a solar cell design by Eq. 11 (Kagan et al. 1999; Shockley and Read 1952),

$$R = \frac{np - n_i^2}{\tau_p \left( n + N_c e^{\frac{E_g - E_i}{k_B T}} \right) + \tau_n \left( p + N_v e^{\frac{E_i}{k_B T}} \right)} \tag{11}$$

Here the  $p$  represents the hole concentrations, whereas the  $n$  represents the concentration of electrons transported through the layers. Again, the  $E_i$  represents the energy levels of the defects in the material layers. The lifespan of electrons and holes,  $n$ ,  $p$ , may be computed using,

$$\tau_{n,p} = \frac{1}{\sigma_{n,p} \cdot V_{th} \cdot N_t} \tag{12}$$

The cross-section area for the carriers to be captured can be denoted by  $\sigma_{n,p}$ , and the thermal velocity is characterized by the  $V_{th}$ . Again, trap defect can be described as the  $N_t$ . However, the relationship between carrier lifetime and diffusion length can be expressed as,

$$L_{n,p} = \sqrt{\frac{\mu_{n,p} k_B T}{q} \tau_{n,p}} \tag{13}$$

where  $\mu_{n,p}$  depicts the mobility of the carriers, and the  $q$  represents the carrier charge. The diffusion lengths for the carriers can vary marginally due to the differences of their effective masses. Raising the defect density value increases the overall recombination rate as the lifespan of the carriers decreases, resulting in a shorter carrier diffusion length and a lowering of the PCE. Due to the higher difficulty rate of achieving a pristine solar panel containing a minimal defect density lower than  $1 \times 10^{14} \text{ cm}^{-3}$ , the optimal value for this investigation is regarded at the density of  $1 \times 10^{15} \text{ cm}^{-3}$  with a PCE 27.36% and an FF value of 82%. The  $J_{sc}$  was near  $24.70 \text{ mA/cm}^2$  and the  $V_{oc}$  is near  $1.35 \text{ V}$ .

### 3.7 Variation of resistance types for proposed structure

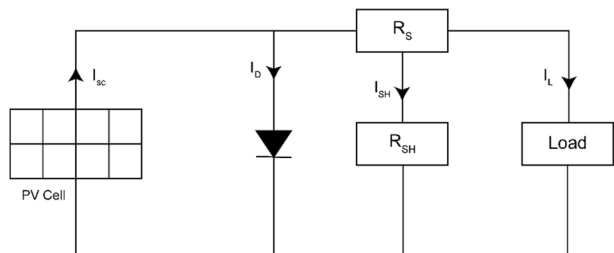
Series resistance is another parameter that significantly impacts a solar cell device’s performance, especially on the Fill Factor and short circuit current density ( $J_{sc}$ ). When we increase the series resistance, the value of the Fill factor also starts to decrease, resulting in short-circuit current reduction. As such, the solar cell’s overall efficiency also starts to reduce. Here, Fig. 13 displays an equivalent circuit of the proposed solar cell where  $R_S$  represents the series resistance value of the model. To have a better understanding of series resistance’s effect on the performance of our device, we can find Eqs. 14 and 15 as follows,

$$I_{SC} = I_0 \left( e^{\frac{V_{oc}q}{nk_B T}} - 1 \right) \tag{14}$$

$$I_{SC} = I_L - I_0 \left( e^{\frac{V_{oc}q}{nk_B T}} - 1 \right) - \frac{V_{oc} + I_{SC}r_s}{R_{sh}} \tag{15}$$

where  $I_L$  is the current induced due to the incident light, short circuit current by  $I_{sc}$  while  $I_0$  represents the reverse saturation current of the device. Again,  $R_{sh}$  depicts the value of

**Fig. 13** Equivalent electrical circuit model of a solar cell



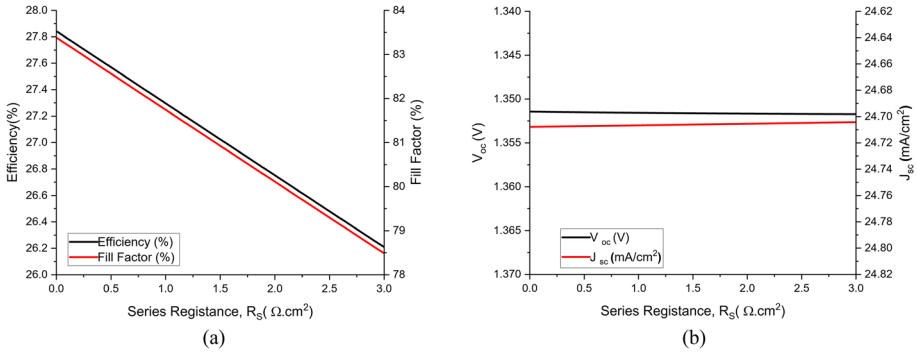


**Fig. 14** Impact of series resistance variation on the proposed cell

shunt resistance. Equations 14 and 15 show that if the value of the  $R_s$  tends to increase, subsequently, the device’s overall efficiency also decreases. Figure 14 depicts the results of series resistance variation over the execution parameters of proposed device model. This study has revealed that the model has performed better in competitively lower series resistance scenarios. But as the resistance increases, every performance parameter drops down at a significant rate.

Again, another significant power loss can occur due to the Shunt Resistance ( $R_{sh}$ ) of a solar cell. The shunt resistance is usually introduced due to manufacturing defects during the fabrication process rather than the poor solar design, making the parameter a critical point to consider for realistic real-life performance estimation. Lower shunt resistance values can provide an alternative path for the carriers to tunnel through, which creates a significant power loss that lowers the performance parameters. The effects can become much more severe in less light situations as lower carriers will be generated, to begin with, while all recombining internally. Figure 15 represents the impact of shunt resistance over the performance parameters of proposed solar cell structure. The graph depicts that initially, at lower shunt resistance, the value of the  $J_{sc}$ , PCE, and FF are at their lower end in terms of values. On the other hand,  $V_{oc}$  is competitively higher. Then

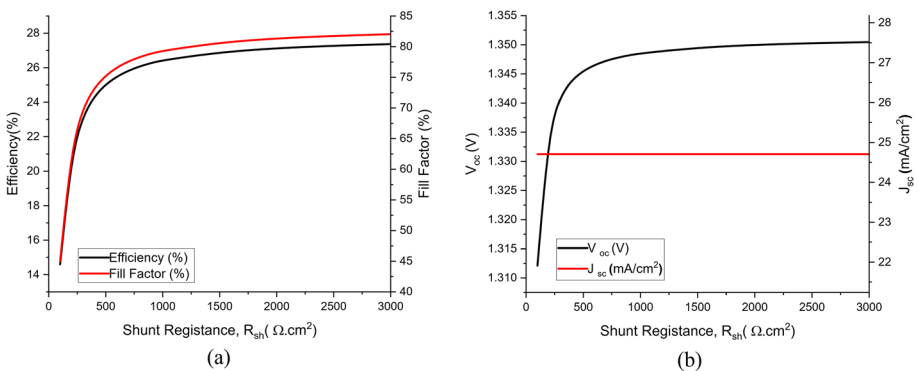


**Fig. 15** Impact of shunt resistance variation on the proposed cell

after a continuous increase in the resistance value, the parameters also improve significantly, increasing the proposed device's stability and reliability.

### 3.8 Variation of operating temperature for the proposed cell

Often the operating temperature of a PSC becomes one of the major limiting factors in the desired performance. The temperature rise can cause due to any form of deformity between the layers caused by the materials due to purity or unwanted error during the fabrication stage. However, any of the reasons may be the occurrence of temperature rise within the cell structure can alter the stability of the device during operation. As the cause of this problem is somewhat unavoidable to an extent, in recent years, researchers are already investing their efforts in uplifting the performance numbers of the perovskites-based optoelectronic devices operating at higher temperature ranges (Li et al. 2018; Ma et al. 2020). To investigate the effects of temperature on solar cell performance, we have altered the operating temperature from 280 to 380 K for proposed solar cell model. Here, Fig. 16 illustrates the negative influence that increasing the operational temperature value has on the device performance. As the temperatures rise, the device's efficiency dips from 28.26 to 23.22% within the transition from 280 to 380 K. Due to an increase in the internal temperature, the diffusion length of the minority carriers starts to shorten, which is one of the primary reasons for falling efficiency. Again, with the rising temperature, the possibility of creating deformation stress among layers becomes eminent, creating interfacial flaws and a deterioration in their interconnectivity. The weak interconnectedness brings up the possibility of the recombination process in the active layer, which also rounds up to the shorter shorter diffusion and higher series resistance, ultimately decreasing the PCE value. Again, the possibility of a solar cell being used at room temperature is much higher in comparison to 280 K, which shows the best results food this study so far. So, to have a near-realistic performance expectation of proposed solar cell structure, we have chosen 300 K to be the optimum choice.

### 3.9 The optimized performance investigation

The study reflects a process of simulating the performance aspects of proposed solar cell architecture by varying various parameters one at a time, keeping the others constant. Then

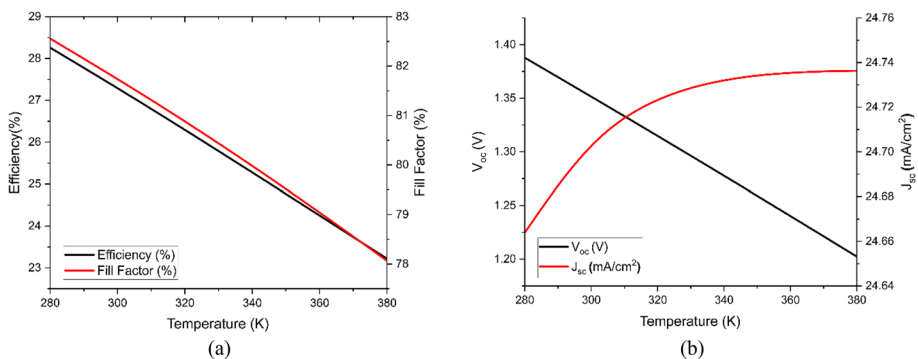


**Fig. 16** Impacts of temperature variation on the proposed cell

**Table 11** Optimized perimeter sets for our proposed perovskite solar cell design

Name	Thickness (nm)	Doping density (cm <sup>-3</sup> )	Defect density (cm <sup>-3</sup> )
FTO	30	1 × 10 <sup>20</sup>	1 × 10 <sup>15</sup>
ZnO	30	1 × 10 <sup>20</sup>	1 × 10 <sup>15</sup>
n-Cs <sub>2</sub> TiCl <sub>6</sub>	100	1 × 10 <sup>16</sup>	1 × 10 <sup>15</sup>
i-Cs <sub>2</sub> TiI <sub>6</sub>	2000	0	1 × 10 <sup>15</sup>
p-Cs <sub>2</sub> TiBr <sub>6</sub>	200	1 × 10 <sup>20</sup>	1 × 10 <sup>15</sup>
NiO	30	1 × 10 <sup>20</sup>	1 × 10 <sup>15</sup>

Operating temperature: 300 K; air mass: 1.5 ATM; LIGHT POWER: 1000 W/m<sup>2</sup>

**Table 12** Performance comparison among proposed cell structure with previous studies

Solar cell	Efficiency (%)	FF (%)	V <sub>oc</sub> (V)	J <sub>sc</sub> (mA/cm <sup>2</sup> )
FTO/ZnO (n)/n-Cs <sub>2</sub> TiCl <sub>6</sub> /i-Cs <sub>2</sub> TiI <sub>6</sub> /p-Cs <sub>2</sub> TiBr <sub>6</sub> /NiO(p)/Pt (proposed)	27.36	82.00	1.35	24.70
Au/PEDOT:PSS/Cs <sub>2</sub> TiBr <sub>6</sub> /TiO <sub>2</sub> /AZO (Moiz et al. 2021)	17.83	70	1.35	18.2
FTO/c-TiO <sub>2</sub> /Cs <sub>2</sub> Ti <sub>0.25</sub> Sn <sub>0.75</sub> Br <sub>6</sub> /Cu <sub>2</sub> O/Au (Shrivastava et al. 2021)	22.13	82.24	1.02	26.24
FTO/TiO <sub>2</sub> /Cs <sub>2</sub> TiBr <sub>6</sub> /CuSCN/Ag (Chakraborty et al. 2021)	13.57	35.95	1.90	19.88
FTO/TiO <sub>2</sub> /Cs <sub>2</sub> TiI <sub>6</sub> /CuSCN/Ag (Chakraborty et al. 2021)	16.31	41	1.74	22.74
FTO/TiO <sub>2</sub> /Cs <sub>2</sub> TiCl <sub>6</sub> /CuSCN/Ag (Chakraborty et al. 2021)	5.50	33.75	1.98	8.23
FTO/TiO <sub>2</sub> /Cs <sub>2</sub> TiF <sub>6</sub> /CuSCN/Ag (Chakraborty et al. 2021)	12.73	38	1.95	17.19

the optimum quantity for that category is finalized depending on the performance parameters like J<sub>sc</sub>, V<sub>oc</sub>, PEC, and FF. The study summarizes the optimization for different absorber scenarios and their thickness investigation, Different ETM and HTM material use and their effects, the influence of the doping, defect densities, effects of the series shunt resistance, and the operating temperature variation. At the end of the whole process, we were able to finalize a solar cell structure as FTO (30 nm)/ZnO(n) (30 nm)/n-Cs<sub>2</sub>TiCl<sub>6</sub> (200 nm)/i-Cs<sub>2</sub>TiI<sub>6</sub> (2 μm)/p-Cs<sub>2</sub>TiBr<sub>6</sub> (100 nm)/NiO(p) (30 nm)/Pt. Here, Table 11 summarizes all the optimized values accumulated from the study up to now and are used for the parameters of optimized device. At the end of the simulation process, we were able to achieve a J<sub>sc</sub> value of 24.70 mA/cm<sup>2</sup>, a V<sub>oc</sub> value of 1.35 V, a PCE value of 27.36% and finally an FF value of 82%. Again Table 12 compares the performance aspects of previously conducted studies with our current work. Figure 17 shows of the J–V curve of finalized device and the quantum efficiency against the wavelength. As per the graph, we can observe that, with a higher wavelength of light, the convection efficiency of the device increases reaching a maximum point. However, this conversion efficiency starts to decrease exponentially for light with a wavelength of more than 680 nm as this light contains lower energy photons than the material bandgap. And light with a wavelength of more than 780 nm cannot produce electrons as this photon’s energy is less than the bandgap of absorbers. So, we can comfortably state that the absorption range for this device is 300–780 nm.

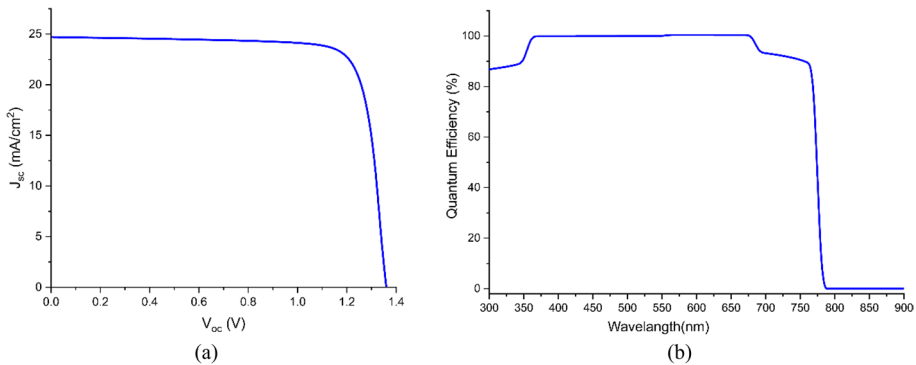


**Fig. 17** Optimized curve for **a** J–V characteristics and **b** quantum efficiency of our intended device design

## 4 Conclusion

The manuscript focuses on optimizing a triple-layer lead-free inorganic halide-based perovskite solar cell structure, focusing on different parameters keeping real-life scenarios in mind, and gaining maximum performance numbers. In the end, the proposed architecture came up to be FTO (30 nm)/ZnO (n) (30 nm)/n-Cs<sub>2</sub>TiCl<sub>6</sub> (100 nm)/i-Cs<sub>2</sub>TiI<sub>6</sub> (2000 nm)/p-Cs<sub>2</sub>TiBr<sub>6</sub> (200 nm)/NiO(p) (30 nm)/Pt which had a total thickness of 2.36 μm. Other parameters like the Air mass and the light power were kept at 1.5 ATM and 1000W/m<sup>2</sup> state, respectively, to have a comparable baseline with other existing studies. The research determined that the performance of a cell structure depending on criteria such as the absorber layers thickness, doping concentration, defect density, and operating temperature, as well as the performance of supporting layers such as TCO, HTL, and ETL. This proposed solar cell archives the highest level of performance under the spectrum range of 300–780 nm wavelength, which covers the visible range due to the considerable material choice of this study. Finally, with all the optimized physical parameters into consideration that presented in Table 11, the structure was able to achieve PV parameters of PCE, V<sub>oc</sub>, J<sub>sc</sub>, and FF values of 27.36%, 24.70 mA/cm<sup>2</sup>, 1.35 V and 82% respectively. Finally, the suggested study is compared to previous studies on performance parameters.

**Acknowledgements** Not applicable.

**Author contributions** The authors contributed equally to the conceptualization and design of the research. RP and MdAI was equally responsible for all aspects of material preparation, data gathering, and analysis for this work.

**Funding** Authors received no financial support for this work's research, authorship, or publication process.

**Availability of data and materials** There are no linked research data sets for this submission.

## Declarations

**Conflict of interest** No relevant financial or non-financial interests are held by the authors of the articles.

**Human rights statement** All procedures conducted in research involving human participants complied with ethical requirements.

**Ethics approval** All types of approval is assured from the authors.

**Consent to participate** Consent is assured from the author of the study.

**Consent for publication** Consent is assured from the author of the study.

## References

- Bal, S., Basak, A., Singh, U.: Numerical modeling and performance analysis of Sb-based tandem solar cell structure using SCAPS-1D. *Opt. Mater.* **127**, 112282 (2022)
- Ball, J., Lee, M., Hey, A., Snaith, H.: Low-temperature processed meso-superstructured to thin-film perovskite solar cells. *Energy Environ. Sci.* **6**(6), 1739–1743 (2013)
- Barbe, J., Tietze, M., Neophytou, M., Murali, B., Alarousu, E., Labban, A., Abulikemu, M., Yue, W., Mohammed, O., McCulloch, I., Amassian, A.: Amorphous tin oxide as a low temperature-processed electron-transport layer for organic and hybrid perovskite solar cells. *ACS Appl. Mater. Interfaces* **9**(13), 11828–11836 (2017)
- Basak, A., Singh, U.: Numerical modelling and analysis of earth abundant  $Sb_2S_3$  and  $Sb_2Se_3$  based solar cells using scaps-1D. *Sol. Energy Mater. Sol. Cells* **230**, 111184 (2021)
- Bhattacharya, S., John, S.: Beyond 30% conversion efficiency in silicon solar cells: a numerical demonstration. *Sci. Rep.* **9**(1), 1–15 (2019)
- Burgelman, M., Nollet, P., Degraeve, S.: Modelling polycrystalline semiconductor solar cells. *Thin Solid Films* **361**, 527–532 (2000)
- Burgelman, M., Decock, K., Khelifi, S., Abass, A.: Advanced electrical simulation of thin film solar cells. *Thin Solid Films* **535**, 296–301 (2013)
- Chakraborty, K., Choudhury, M., Paul, S.: Numerical study of  $Cs_2TiX_6$ -based perovskite solar cell using SCAPS-1D device simulation. *Sol. Energy* **194**, 886–892 (2019)
- Chakraborty, K., Choudhury, M., Paul, S.: Study of physical, optical, and electrical properties of cesium titanium (IV)-based single halide perovskite solar cell. *IEEE J. Photovolt.* **11**(2), 386–390 (2021)
- Chaudhary, N., Chaudhary, R., Kesari, J.P., Patra, A., Chand, S.: Copper thiocyanate (CuSCN): an efficient solution-processable hole transporting layer in organic solar cells. *J. Mater. Chem. C* **3**(45), 11886–11892 (2015)
- Chen, M., Ju, M., Carl, A., Zong, Y., Grimm, R., Gu, J., Zeng, X., Zhou, Y., Padture, N.: Cesium titanium(IV) bromide thin films based stable lead-free perovskite solar cells. *Joule* **2**(3), 558–570 (2018)
- Correa-Baena, J., Anya, M., Lozano, G., Tress, W., Domanski, K., Saliba, M., Matsui, T., Jacobsson, T., Calvo, M., Abate, A., Grätzel, M.: Unbroken perovskite: interplay of morphology, electro-optical properties, and ionic movement. *Adv. Mater.* **28**(25), 5031–5037 (2016)
- Giustino, F., Snaith, H.: Toward lead-free perovskite solar cells. *ACS Energy Lett.* **1**(6), 1233–1240 (2016)
- Grätzel, M.: The light and shade of perovskite solar cells. *Nat. Mater.* **13**(9), 838–842 (2014)
- Huang, L., Sun, X., Li, C., Xu, R., Xu, J., Du, Y., Wu, Y., Ni, J., Cai, H., Li, J., Hu, Z.: Electron transport layer-free planar perovskite solar cells: further performance enhancement perspective from device simulation. *Sol. Energy Mater. Sol. Cells* **157**, 1038–1047 (2017)
- Ju, M.G., Chen, M., Zhou, Y., Garces, H.F., Dai, J., Ma, L., Padture, N.P., Zeng, X.C.: Earth-abundant nontoxic titanium (IV)-based vacancy-ordered double perovskite halides with tunable 1.0 to 1.8 eV bandgaps for photovoltaic applications. *ACS Energy Lett.* **3**(2), 297–304 (2018)
- Kagan, C., Mitzi, D., Dimitrakopoulos, C.: Organic-inorganic hybrid materials as semiconducting channels in thin-film field-effect transistors. *Science* **286**(5441), 945–947 (1999)
- Ke, W., Kanatzidis, M.: Prospects for low-toxicity lead-free perovskite solar cells. *Nat. Commun.* **10**(1), 1–4 (2019)
- Kim, H., Lim, K., Lee, T.: Planar heterojunction organometal halide perovskite solar cells: roles of interfacial layers. *Energy Environ. Sci.* **9**(1), 12–30 (2016)
- Kour, R., Arya, S., Verma, S., Gupta, J., Bandhoria, P., Bharti, V., Datt, R., Gupta, V.: Potential substitutes for replacement of lead in perovskite solar cells: a review. *Global Chall.* **3**(11), 1900050 (2019)
- Kumari, P., Punia, U., Sharma, D., Srivastava, A., Srivastava, S.: Enhanced photovoltaic performance of PEDOT: PSS/Si heterojunction solar cell with ZnO BSF layer: a simulation study using scaps-1D. *SILICON* **15**, 2099–2112 (2022)
- Li, Y., Shi, Z., Lei, L., Zhang, F., Ma, Z., Wu, D., Xu, T., Tian, Y., Zhang, Y., Du, G., Shan, C.: Highly stable perovskite photodetector based on vapor-processed micrometer-scale  $CsPbBr_3$  microplatelets. *Chem. Mater.* **30**(19), 6744–6755 (2018)
- Lin, L., Jiang, L., Qiu, Y., Yu, Y.: Modeling and analysis of HTM-free perovskite solar cells based on ZnO electron transport layer. *Superlattices Microstruct.* **104**, 167–177 (2017)



- Ma, Z., Shi, Z., Qin, C., Cui, M., Yang, D., Wang, X., Wang, L., Ji, X., Chen, X., Sun, J., Wu, D.: Stable yellow light-emitting devices based on ternary copper halides with broadband emissive self-trapped excitons. *ACS Nano* **14**(4), 4475–4486 (2020)
- Mandadapu, U., Vedanayakam, S., Thyagarajan, K., Reddy, M., Babu, B.: Design and simulation of high efficiency tin halide perovskite solar cell. *Int. J. Renew. Energy Res* **7**(4), 1603–1612 (2017)
- Moiz, S., Alahmadi, A., Aljohani, A.: Design of a novel lead-free perovskite solar cell for 17.83% efficiency. *IEEE Access* **9**, 54254–54263 (2021)
- Moiz, S., Albadwani, S., Alshaikh, M.: Towards highly efficient cesium titanium halide-based lead-free double perovskites solar cell by optimizing the interface layers. *Nanomaterials* **12**(19), 3435 (2022)
- Moustafa, M., Alzoubi, T.: Numerical study of CDTE solar cells with p-MoTe2 TMDC as an interfacial layer using SCAPS. *Mod. Phys. Lett. B* **32**(23), 1850269 (2018)
- Parida, B., Iniyar, S., Goic, R.: A review of solar photovoltaic technologies. *Renew. Sustain. Energy Rev.* **15**(3), 1625–1636 (2011)
- Paul, S., Grover, S., Repins, I.L., Keyes, B.M., Contreras, M.A., Ramanathan, K., Noufi, R., Zhao, Z., Liao, F., Li, J.V.: Analysis of back-contact interface recombination in thin-film solar cells. *IEEE J. Photovolt.* **8**(3), 871–878 (2018)
- Rai, S., Pandey, B., Dwivedi, D.: Modeling of highly efficient and low cost CH<sub>3</sub>NH<sub>3</sub>Pb(I<sub>1-x</sub>Cl<sub>x</sub>)<sub>3</sub> based perovskite solar cell by numerical simulation. *Opt. Mater.* **100**, 109631 (2020)
- Raj, A., Kumar, M., Kumar, A., Anshul, A.: An optimized lead-free formamidine Sn-based perovskite solar cell design for high power conversion efficiency by SCAPS simulation. *Opt. Mater.* **108**, 110213 (2020)
- Raj, A., Kumar, M., Anshul, A.: Recent progress in cesium-based lead-free halide double perovskite materials for photovoltaic applications. *Phys. Status Solidi A* **219**, 2200425 (2022)
- Sabbah, H.: Numerical simulation of 30% efficient lead-free perovskite CsSnGeI<sub>3</sub>-based solar cells. *Materials* **15**(9), 3229 (2022)
- Saive, R.: Light trapping in thin silicon solar cells: a review on fundamentals and technologies. *Prog. Photovolt. Res. Appl.* **29**(10), 1125–1137 (2021)
- Sawicka-Chudy, P., Sibiński, M., Wisz, G., Rybak-Wilusz, E., Cholewa, M.: Numerical analysis and optimization of Cu<sub>2</sub>O/TiO<sub>2</sub>, CuO/TiO<sub>2</sub>, heterojunction solar cells using scaps. *J. Phys. Conf. Ser.* **1033**(1), 012002 (2018)
- Sawicka-Chudy, P., Starowicz, Z., Wisz, G., Yavorskyi, R., Zapukhlyak, Z., Bester, M., Sibiński, M., Cholewa, M.: Simulation of TiO<sub>2</sub>/CuO solar cells with scaps-1D software. *Mater. Res. Express* **6**(8), 085918 (2019)
- Schloemer, T., Christians, J., Luther, J., Sellinger, A.: Doping strategies for small molecule organic hole-transport materials: impacts on perovskite solar cell performance and stability. *Chem. Sci.* **10**(7), 1904–1935 (2019)
- Shockley, W., Queisser, H.: Detailed balance limit of efficiency of p–n junction solar cells. *J. Appl. Phys.* **32**(3), 510–519 (1961)
- Shockley, W., Read, W., Jr.: Statistics of the recombination of holes and electrons. *Phys. Rev.* **87**(5), 835 (1952)
- Shrivastava, P., Kavaipatti, B., Bhargava, P.: First principles study of Cs<sub>2</sub>Ti<sub>1-x</sub>M<sub>x</sub>Br<sub>6</sub> (M = Pb, Sn) and numerical simulation of the solar cells based on Cs<sub>2</sub>Ti<sub>0.25</sub>Sn<sub>0.75</sub>Br<sub>6</sub> perovskite. *Int. J. Energy Res.* **45**(5), 8049–8060 (2021)
- Singh, P., Rai, S., Lohia, P., Dwivedi, D.: Comparative study of the CZTS, CuSbS<sub>2</sub> and CuSbSe<sub>2</sub> solar photovoltaic cell with an earth-abundant non-toxic buffer layer. *Sol. Energy* **222**, 175–185 (2021)
- Snaith, H., Green, M., Ho-Baillie, A.: The emergence of perovskite solar cells. *Nat. Photonics* **8**(7), 506–514 (2014)
- Song, T., Yokoyama, T., Aramaki, S., Kanatzidis, M.: Performance enhancement of lead-free tin-based perovskite solar cells with reducing atmosphere-assisted dispersible additive. *ACS Energy Lett.* **2**(4), 897–903 (2017)
- Widianto, E., Rosa, E., Triyana, K., Nursam, N., Santoso, I.: Performance analysis of carbon-based perovskite solar cells by graphene oxide as hole transport layer: experimental and numerical simulation. *Opt. Mater.* **121**, 111584 (2021)

**Publisher's Note** Springer Nature remains neutral with regard to jurisdictional claims in published maps and institutional affiliations.

Springer Nature or its licensor (e.g. a society or other partner) holds exclusive rights to this article under a publishing agreement with the author(s) or other rightsholder(s); author self-archiving of the accepted manuscript version of this article is solely governed by the terms of such publishing agreement and applicable law.